

# Dynamic features of Cu-ceria interface under CO<sub>2</sub> Hydrogenation to Methanol

Yuanyuan Li<sup>[a,\*]</sup>, Yiming Chen<sup>[b]</sup>, Haohong Song<sup>[b]</sup>, Kinga A. Unocic<sup>[c,h]</sup>, Jorge Perez-Aguilar<sup>[d]</sup>, Jiyun Hong<sup>[d]</sup>, Adam S. Hoffman<sup>[d]</sup>, Jorge Moncada<sup>[e]</sup>, Jeongjin Kim<sup>[e]</sup>, Luke Daemen<sup>[f]</sup>, Yongqiang Cheng<sup>[f]</sup>, Caiqi Wang<sup>[a]</sup>, Sanjaya D. Senanayake<sup>[e]</sup>, Simon R. Bare<sup>[d]</sup>, De-en Jiang<sup>[b, g]</sup>, Zili Wu<sup>[a, c]</sup>

[a] Chemical Sciences Division, Oak Ridge National Laboratory, Oak Ridge, Tennessee 37831, United States

[b] Interdisciplinary Materials Science, Vanderbilt University, Nashville, Tennessee, 37235, United States

[c] Center for Nanophase Materials Sciences, Oak Ridge National Laboratory, Oak Ridge, Tennessee 37831, United States

[d] Stanford Synchrotron Radiation Lightsource, SLAC National Accelerator Laboratory, Menlo Park, California 94025, United States

[e] Chemistry Division, Brookhaven National Laboratory, Upton, New York 11973, United States

[f] Neutron Scattering Division, Oak Ridge National Laboratory, Oak Ridge, Tennessee 37831, United States

[g] Department of Chemical and Biomolecular Engineering, Vanderbilt University, Nashville, Tennessee, 37235, United States

[h] Department of Materials Science and Engineering, North Carolina State University, Raleigh, 27606, North Carolina, United States

\* Corresponding author

E-mail for Y. L.: [liy4@ornl.gov](mailto:liy4@ornl.gov)

## Abstract

It is generally accepted that metal-support interaction is very important for CO<sub>2</sub> hydrogenation to methanol, but little has been revealed about the feature of interfacial active sites under the real reaction conditions since there are only limited techniques that can be applied under high pressure conditions. In this work, by combining multiple in situ and operando techniques on a model Cu/ceria catalyst, we have tracked Cu and ceria sites for methanol formation. Under the reaction condition, it is found that upon reaching the reaction temperature, oxidized Cu species in the as-synthesized catalyst immediately changes into metallic Cu species. Following it, it's the gradual formation of methanol, the changing rate of which coincides with the formation of a unique Ce<sup>3+</sup> species. The combined experimental results and density functional theory (DFT) calculations have determined that the formed Ce<sup>3+</sup> sites driven by the reaction condition are bound to hydrides, adsorbed carbonate species, and interfacial active Cu sites. The Cu-ceria interaction in this complex moiety is weak and can be easily disturbed with reaction environment variations, leading to dynamic changes at the interface upon the hydrogenation of active carbonate intermediates, that are precursors for the formation of methanol. The formation of this unique Cu-Ce<sup>3+</sup> interface and its dynamicity lead to an increase of methanol selectivity from less than 20% to 60%. These results suggest that reactant-derived species (H<sup>-</sup> and carbonate in this work) can be essential components of the active center with the functions of manipulating metal-oxide interaction and directing reaction pathways.

Keywords: CO<sub>2</sub> hydrogenation to methanol, operando studies, Cu/ceria, cerium hydride, carbonate intermediates, neutron scattering, high energy resolution fluorescence detected X-ray absorption

## Introduction

The reaction of CO<sub>2</sub> hydrogenation has been studied for decades due to its importance in producing valuable chemicals yet presented challenges in determining and designing highly selective sites for the necessary high pressure catalytic conditions. Taking CO<sub>2</sub> hydrogenation to methanol as an example, in industry, the produced methanol can be used as a fuel or to produce many other chemicals (such as formaldehyde, acetic acid, and plastics). However, in practice, along with this reaction is the competing reverse water gas shift reaction, which leads to the formation of the primary byproduct, CO. As a result, currently, there are few systems that show high methanol selectivity and yield in CO<sub>2</sub> hydrogenation, as summarized in several recent reviews.<sup>1,2</sup>

To improve the selectivity of methanol, many efforts have been made to reveal the nature of active sites for methanol synthesis from CO<sub>2</sub> hydrogenation. Among those, however, there are limited studies focusing on working catalysts under the realistic high pressure reaction condition. Consequently, the obtained information is usually ambiguous and there are even intense debates about the active structure/phase such as in the commercial methanol synthesis catalyst Cu/ZnO/Al<sub>2</sub>O<sub>3</sub> (CZA). For instance, Kattel *et al.* found that ZnCu became as active as ZnO/Cu only after it undergoes surface oxidation to form ZnO.<sup>3</sup> However, based on the XAS data of the Cu/ZnO/Al<sub>2</sub>O<sub>3</sub> catalyst, Zabilskiy *et al.* found that Zn existed in two species (ZnO and CuZn alloy) in H<sub>2</sub> condition (15 bar and 533 K) and upon switching to CO<sub>2</sub> hydrogenation, a new Zn formate species showed up.<sup>4</sup> Regarding Cu, the reported active phase/site includes monometallic Cu, CuZn alloy, Cu surface defects, or Cu<sup>1+</sup> ions.<sup>5-7</sup>

Although contradicting, these previous results, together with many other studies, pointed out the importance of Cu-oxide interface for methanol synthesis.<sup>8-13</sup> Inspired by these, we recently engineered Cu/BaTiO<sub>3</sub> by introducing hydride anions into the support and by doing so, the methanol selectivity and yield were significantly improved, suggesting that supports do have strong effects on activity and selectivity.<sup>14</sup> However, in that work, we did not observe support effects on the structure of Cu nanoparticle under the reaction condition.<sup>14</sup> In fact, in most of previous reports, changes were not observed on Cu as well. As a result, there are no/little discussion on the nature of active sites at the Cu-support interface.<sup>15</sup> These results from our and other groups have puzzled us: *is it because the size of Cu species become too large under high pressure CO<sub>2</sub> hydrogenation that most in situ/operando average techniques cannot detect the subtle change of active sites? Or are there other reasons that are unexpected or beyond intuition?*

Driven by these questions, we aim to provide detailed information about what is happening at the metal-support interface under the reaction conditions for CO<sub>2</sub> hydrogenation. To achieve this goal, we will need to address the challenges associated with high pressure conditions. First, many techniques that are crucial for surface or catalysis studies, such as electron-based imaging microscopy (transmission electron microscopy or scanning transmission electron microscopy – TEM/STEM) and soft X-ray based spectroscopy (such as X-ray photoelectron spectroscopy – XPS) currently cannot be adapted to high pressure measurements. Second, Infrared (IR) spectroscopy can be used to detect surface intermediates and surface metal species/sites with the presence of probe CO molecules. For CO<sub>2</sub> hydrogenation to methanol over Cu-based catalysts, the

primary byproduct is CO under typical reaction temperatures ( $\leq 300^\circ\text{C}$ ) and by taking advantage of it, in principle, the information about surface metal species/sites can be obtained under reaction conditions. However, under high pressure  $\text{CO}_2$  hydrogenation, the signals of gas phase  $\text{CO}_2$  dominate and even show bands in the characteristic range of adsorbed CO on metal sites, making it difficult to reveal the surface metal sites under reaction conditions.<sup>16</sup> Third, hard X-ray based techniques especially X-ray absorption spectroscopy (XAS) is the primary technique that has been used in several studies to investigate the structure of catalysts under high pressure reaction conditions.<sup>4, 17-20</sup> The drawback of XAS is that it provides global average results. To detect changes, its sensitivity to the change of minority sites should be improved. Fourth, many developed systems for  $\text{CO}_2$  hydrogenation to methanol are quite complex: for instance,  $\text{Cu/ZnO/Al}_2\text{O}_3$ , which is used in industry for methanol synthesis from syngas, is considered as a benchmark for  $\text{CO}_2$  hydrogenation to methanol, but its structure involves multiple interfaces and sites, making it difficult to pick out the information only from active sites.

To address the above-mentioned challenges, in this work, we apply in situ/operando techniques including XAS, neutron scattering and IR spectroscopy on a simplified model system – Cu/ceria to correlate its structural evolution with the time-dependent methanol selectivity and yield during  $\text{CO}_2$  hydrogenation. The Cu/ceria system shows comparable performance with that of commercial  $\text{Cu/ZnO/Al}_2\text{O}_3$ .<sup>8</sup> In this study, under the similar testing condition, the methanol selectivity and yield over Cu/ceria are 60 % and 160 mg/h/g<sub>Cu</sub>, respectively (**Fig. S1**) while for commercial  $\text{Cu/ZnO/Al}_2\text{O}_3$ , they are 48 % and 230 mg/h/g<sub>Cu</sub>.<sup>14</sup> To improve the sensitivity of XAS, we combine conventional and high energy resolution fluorescence detected (HERFD) – XAS. To detect the surface Cu sites by using IR, we keep the spent catalyst (spent means the catalyst has been exposed to the reaction condition) sealed and perform CO probed diffuse reflectance infrared Fourier transformed spectroscopy (DRIFTS). For techniques that cannot be used under high pressure conditions (such as Ambient pressure (AP) – XPS and TEM), we mimic reactive conditions to provide complementary information on the active sites. By applying these strategies and with the assistance of DFT calculations and simulations, the nature of the interfacial active center for the formation of methanol and its dynamic change under the reaction is compellingly revealed.

## Experimental Section

### Sample preparation

The Cu/ceria sample was prepared by dispersing 2.49 g cerium(IV) oxide nanopowder (<25 nm) in a solution of 3.0 g urea and 25 mL of water. The desired amount (5.01 ml) of Cu precursor solution (Copper(II) nitrate trihydrate in water, approx. 2.6 wt.% Cu) was then added. The mixture was sealed in a round-bottom flask and stirred for 24 hours in an oil bath at 95 °C. Following this deposition process, the samples were separated and washed by 3 cycles of centrifuging/redispersing in DI water to remove the residual ions from precursors. After drying overnight in an oven at 80 °C, the samples were crushed into powders and calcined at 500 °C for 5 hours. The resulting Cu loading of the sample was measured by Inductively Coupled Plasma (ICP) elemental analysis and determined to be 3.2 wt%.

## **Catalytic performance tests**

For the catalytic performance test, about 0.2 g catalyst mixed with 1.0 g quartz sand was loaded to the reactor (PID Eng & Tech) and a mixture of gas composed of 72% H<sub>2</sub>, 24% CO<sub>2</sub>, and 4% Ar was introduced at the flow rate of 15.5 mL/min. The catalytic performance was tested at 220 °C and 30 bar. An on-line gas chromatograph (Agilent) equipped with a flame ionization detector (FID) and a thermal conductivity detector (TCD) was used to analyze all products. A Porapak Q and a Carboxen column were utilized for separating the reactants and products.

## **D<sub>2</sub> Temperature-Programmed Reduction (TPR)**

About 100 mg of used sample was loaded into a quartz reactor and pretreated under a He flow (30 mL/min) at 120 °C for 1 h. The pretreatment was to remove physisorbed water. After pretreatment, the reactor was cooled to 50 °C, and the gas feed was switched to D<sub>2</sub> (30 mL/min) for purging 1 hour. The temperature was then increased from 50 °C to 500 °C at a heating rate of 10 °C/min. The effluent gas of HD from exchange between gas phase D<sub>2</sub> and mostly the hydride (H<sup>-</sup>) species in ceria was continuously monitored using a mass spectrometer (Pfeiffer Vacuum). For comparison, the fresh catalyst was pretreated and studied in a same manner to monitor the exchange between gas phase D<sub>2</sub> and surface hydroxyls (OH).

## **Ambient-Pressure X-ray Photoelectron Spectroscopy**

Ambient pressure X-ray photoelectron spectroscopy (AP-XPS) studies were conducted using a SPECS chamber equipped with a PHOIBOS 150 EP MCD-9 analyzer (Chemistry Division, BNL) using a Mg K $\alpha$  anode as x-ray source (energy resolution 0.4eV, pass energy 30 eV).<sup>21</sup> XPS spectra were collected at UHV and 30 mTorr of H<sub>2</sub> using a 300  $\mu$ m aperture cone and a differentially pumped analyzer electron optics for collection of electrons at elevated pressure while keeping the analyzer under near UHV.<sup>22</sup> Cu2p and Ce3d spectra were measured under reducing conditions at room temperature, 150, and 250°C.

## **Neutron scattering**

The inelastic neutron scattering spectrum was collected at VISION beamline. VISION is an inverted geometry spectrometer used for neutron vibrational spectroscopy at the pulsed spallation neutron source (SNS) at Oak Ridge National Laboratory. VISION uses the time-of-flight technique to measure the energy of neutrons incident on the sample. The final neutron energy is set by Bragg reflection on pyrolytic graphite analyzers. The dynamic range is 0 to ~6000 cm<sup>-1</sup>. The energy resolution in that range is approximately 1 to 1.5%.<sup>23</sup> The sample was loaded in a stainless steel sample holder (19 mm diameter x 60 mm height) sealed with copper gaskets. A capillary tube connected to the sample holder allowed for evacuation and gas loading. The sample was heated to

120 °C under vacuum for one hour to remove any adsorbed water and gases. This sample was cooled to 5K at the VISION beam line and a neutron vibrational spectrum was collected for 2 hours to serve as background for the subsequent measurements. This sample was then warmed up to room temperature and exposed to a CO<sub>2</sub>:H<sub>2</sub> gas mixture (1:3 molar ratio, 30 bar) at 220 °C for 3 hours. The sample was then cooled to 120 °C and decreased to atmospheric pressure, and purged with helium for several minutes to remove physisorbed species. The sample was then cooled to 5K and a neutron vibrational spectrum was collected for 3 hours.

### **In situ STEM measurement**

*In situ* closed gas cell microscopy was conducted using an aberration-corrected JEOL 2200FS operated at 200kV and the Protochips Atmosphere™ gas reaction system for the *in situ* STEM experiments. Protochips Atmosphere system allows to perform study on a range of material systems in response to temperatures up to 1000°C and pressures up to 1 atm (760 Torr) within a reactive gas environment to study the structural and chemical changes of Cu/ceria sample. Samples were drop cast on the silicon nitride window of a Protochips™ E-chip heater chip. The gas-cell was flushed three times with nitrogen from 100 to 0.1 Torr to ensure there was no O<sub>2</sub> present in the system. The pressure was then set to 760 Torr and the gas-cell was filled with 100% H<sub>2</sub>. Due to the geometry of the manifold that holds the supply gas tanks and continuous flow of the H<sub>2</sub> during the experiment, there was a pressure drop with time that was constantly reset. Temperature was brought from room temperature to 400°C under flowing 100% H<sub>2</sub> at 5°C/min. The exposure to the electron beam was minimized by blinking the beam exposure.

### **In situ/operando XAS measurement**

The Cu K edge and Ce L<sub>3</sub> edge conventional XAS spectra were collected at the beamline 4-2 and 9-3, the HERFD-XAS spectra were collected at the beamline 15-2 of the Stanford Synchrotron Radiation Lighthouse (SSRL) at the SLAC National Laboratory at SSRL. The sample powder was loaded to a quartz capillary (0.98 mm I.D. and 0.02 mm wall thickness) reactor, which can hold pressure up to 20 bar.<sup>24</sup> The XAS data were collected in fluorescence mode. For the measurement of Ce L<sub>3</sub> edge XAS data, the sample powder was diluted with silica (1:10). For the data plotted in **Fig. 1**, the as-prepared catalyst was exposed to the reaction condition (CO<sub>2</sub>:H<sub>2</sub>=1:3; 20 bar). Subsequently, the reaction temperature was increased to 220 °C at the ramp rate of 10 °C/min. Once the temperature reached 220 °C, the time-dependent XAS spectra were collected. For the data plotted in **Fig. 2**, the spectra were first collected under the reaction condition (CO<sub>2</sub>:H<sub>2</sub>=1:3; 20 bar, 220 °C). Secondly, the reaction temperature was drop to room temperature (CO<sub>2</sub>:H<sub>2</sub>=1:3; 20 bar, RT). Thirdly, H<sub>2</sub> was replaced with He (CO<sub>2</sub>:He=1:3; 20 bar, RT). For reference, the spectra of the as-prepared catalyst were also collected.

### **DRIFTS measurement**

IR measurements were performed by using a Bruker FTIR spectrometer equipped with a Praying Mantis High Temperature Reaction Chambers and an MCT detector. The as-synthesized catalyst weighing approximately 60 mg was loaded into the DRIFTS cell. Each spectrum was collected with 128 scans at a resolution of  $4\text{ cm}^{-1}$ . For the switch experiments, under the steady state reaction condition ( $220^\circ\text{C}$ , 30 bar), the reactants ( $24\%^{12}\text{CO}_2/72\%\text{H}_2/4\%\text{Ar}$ ) were switched to  $24\%^{13}\text{CO}_2/72\%\text{H}_2/4\%\text{He}$ , Ar, or  $\text{H}_2$ . During the switch, the IR spectra were collected continuously to follow any spectral changes. For the CO-DRIFTS experiment, after the reaction condition ( $24\%\text{CO}_2/72\%\text{H}_2/4\%\text{Ar}$  reaction at  $220^\circ\text{C}$  and 30 bar), the reactants were flushed away by He, the temperature was dropped to RT, the pressure was decreased to ambient pressure, and subsequently, CO was introduced to detect the surface accessible Cu sites. When the spectra reached a steady state, CO was flushed away by He to check reversibility. During CO adsorption and desorption, the IR spectra were collected continuously.

### **CO pulse adsorption experiment**

The CO pulse adsorption experiment was conducted by using an AMI-300 Chemisorption Analyzer (Altamira Instruments). Approximately 200 mg of the used catalyst was loaded into a quartz reactor. Three types of pulse experiments were performed. First, the spent catalyst was pretreated under a He flow ( $20\text{ mL/min}$ ) at  $120^\circ\text{C}$  for 1 h to remove physically adsorbed species and water. After pretreatment, the reactor was cooled to  $50^\circ\text{C}$  and maintained under a He flow ( $20\text{ mL/min}$ ). Pulses of 2 vol% CO/He were introduced into the reactor using a  $0.514\text{ mL}$  injection loop. By doing this experiment, we can estimate number of exposed copper sites from CO adsorption on the spent catalyst. Second, after 10 pulses of 2 vol% CO/He, the gas flow was switched to  $\text{H}_2$ , and the reactor was heated to  $220^\circ\text{C}$  and held for 1 h. By doing this, we can remove some of the surface adsorbates. The reactor was then cooled to  $50^\circ\text{C}$ , and the CO pulse sequence was repeated under the same conditions. By doing this experiment, we can estimate CO adsorption on the spent catalyst with reactive surface species being removed. Third, the reactor was again pretreated in  $\text{H}_2$  at  $220^\circ\text{C}$  for 1 h, followed by cooling to  $50^\circ\text{C}$  under He flow ( $20\text{ mL/min}$ ). Ten pulses of  $\text{CO}_2$  were then introduced into the reactor, followed by another 10 pulses of 2 vol% CO/He. By doing this, we can study the competitive adsorption of CO and  $\text{CO}_2$ . For all pulse experiments, the effluent gas was continuously monitored by a thermal conductivity detector (TCD).

### **DFT computation**

Density functional theory (DFT) calculations were performed using the Vienna Ab initio Simulation Package (VASP).<sup>25, 26</sup> The Perdew–Burke–Ernzerhof (PBE) functional of generalized-gradient approximation (GGA) was employed for electron exchange and correlation.<sup>27</sup> The electron-core interaction was modeled using the projector-augmented wave method (PAW).<sup>28, 29</sup> The vdW-DF functional<sup>30</sup> was used to improve the prediction of CO adsorption energies on the copper cluster.<sup>31</sup> The on-site Coulomb interaction was considered by employing the DFT+U

method by Dudarev, et al. with a U value of 4.5 eV for Ce 4f localized electrons based on previous studies.<sup>32-34</sup> Plane-wave kinetic energy cutoff was set to 500 eV to treat the valence electrons.

The bulk cerium oxyhydride with a composition of CeO<sub>1.75</sub>H<sub>0.25</sub> was modeled by replacing one O atom in the Ce<sub>4</sub>O<sub>8</sub> fluorite-structure unit cell with H; the optimized lattice parameter is 5.47 Å. Then the (111) surface of CeO<sub>1.75</sub>H<sub>0.25</sub> was created with three CeO<sub>1.75</sub>H<sub>0.25</sub> sandwich layers with a vacuum layer of 15 Å in thickness. The bottom CeO<sub>1.75</sub>H<sub>0.25</sub> sandwich layer was fixed during geometry optimization. The Brillouin zone of the surface slab was sampled using the Monkhorst–Pack scheme, with a (2 × 2 × 1) k-mesh. Next, a Cu<sub>12</sub> cluster was placed on the surface, followed by a carbonate species from CO<sub>2</sub> adsorption and reaction with a surface O site. The adsorption energy is calculated by:

$$E_{ads} = E_{slab/CO} - E_{slab} - E_{CO},$$

where  $E_{slab/CO}$  represents the system energy of slab with the adsorbed CO;  $E_{slab}$  and  $E_{CO}$  represent the energies of the clean slab and the gas phase CO in a large box, respectively. A scaling factor of 1.03 based on the gas phase CO vibrational frequency was used to calibrate the adsorbed CO frequency. The equilibrium structures were optimized with a force convergence criterion of 0.01 eV/Å. The vibrational frequencies were computed using the finite-difference displacement with a displacement of 0.02 Å for the C and O atoms only. Dipole corrections were included. Frequency calculations were performed using both the PBE+U and HSE06 functionals to assess the influence of electron exchange–correlation on the computed vibrational frequencies.

## Results and Discussion

### Correlated Formation of Methanol and Ce<sup>3+</sup> hydride

The time-resolved Cu K edge and Ce L<sub>3</sub> edge XAS spectra under the reaction condition (CO<sub>2</sub>:H<sub>2</sub> = 1:3; 20 bar; 220 °C) are collected to track the change of Cu/ceria catalyst. As shown in **Fig. S2**, upon heating the Cu/ceria catalyst under the reaction environment at 20 bar from RT to 220 °C, oxidized Cu species is readily reduced to Cu metal. Thereafter the time-dependent changes of Cu K edge spectra at 220 °C are not observed. Based on the EXAFS data analysis (**Fig. S3** and **Table S1**), during the reaction, the average coordination number (CN) of Cu–Cu is 10.8 ± 0.3, smaller than that in Cu foil (12); the average bond distance of Cu–Cu is 2.534 ± 0.002 Å, shorter than that in Cu foil (2.542 ± 0.002 Å), suggesting the formation of nanosized Cu nanoparticles under the reaction condition. The estimated average particle size of Cu nanoparticles is ~4.5 nm under the high-pressure reaction condition.<sup>35</sup> This changing trend of Cu is similar to those previously observed in other Cu-based systems.<sup>4, 14, 17</sup>

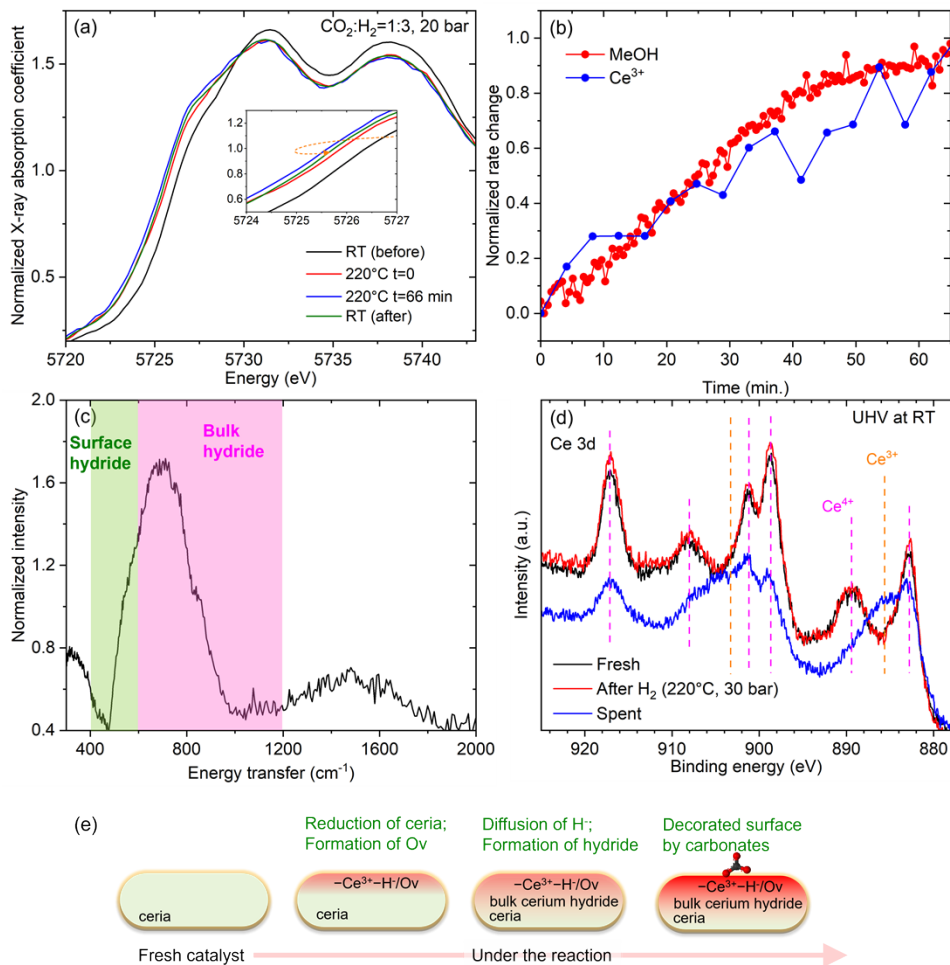


**Figure 1.** (a) The Ce  $L_3$  edge XANES spectra of Cu/ceria before ( $\text{CO}_2:\text{H}_2 = 1:3$ ; 20 bar; RT), during ( $\text{CO}_2:\text{H}_2 = 1:3$ ; 20 bar; 220 °C), and after ( $\text{CO}_2:\text{H}_2 = 1:3$ ; 20 bar; RT) the reaction. (b) The normalized changing rate of methanol and  $\text{Ce}^{3+}$  species. (c) The in-situ inelastic neutron scattering spectrum of the spent Cu/ceria. (d) The Ce 3d XPS spectra of the fresh,  $\text{H}_2$ -treated, and the spent Cu/ceria catalyst. All catalysts have been exposed to air for 4 months. (e) Changes of ceria under the reaction. Note, for a ceria hydride, hydrogen is  $\text{H}^-$ .

Interestingly, the time-dependent change is observed from Ce  $L_3$  edge XANES spectra (**Fig. 1a, S4**). There is an increase in the concentration of  $\text{Ce}^{3+}$  at longer reaction time, as evidenced by the increased shoulder peak at about 5727 eV.<sup>36-38</sup> Cooling the sample to the room temperature causes the reversed shift of the Ce  $L_3$  edge. The linear combination fitting is performed on the time-resolved XANES spectra (**Fig. S4**). The increasing rate of  $\text{Ce}^{3+}$  is similar to that of methanol (**Fig. 1b**), detected by using an on-line Hiden mass spectrometer (**Fig. S5**). The coincident change of  $\text{Ce}^{3+}$  and methanol selectivity/yield indicates a crucial role of oxide supports in determining the methanol selectivity and a transformation of some ceria sites from CO selective to methanol selective. Since ceria itself is barely active under the same reaction condition, these developed  $\text{Ce}^{3+}$  sites must interact with interfacial Cu sites.

The in-situ inelastic neutron scattering spectrum (**Fig. 1c**) collected over the Cu/CeO<sub>2</sub> catalyst after being exposed to the reaction condition for 3 hours (CO<sub>2</sub>:H<sub>2</sub> = 1:3; 30 bar; 220 °C) shows the existence of surface and bulk Ce hydrides (in which hydrogen is H<sup>-</sup>) in the spent Cu/ceria, as evidenced by the pronounced peak ranging from 500 to 1000 cm<sup>-1</sup>.<sup>39</sup> Basing on D<sub>2</sub> TPR experiments (**Fig. S6**), the ratio between the surface and bulk hydrides is about 0.3 and surface hydrides likely play a larger role than bulk ones in CO<sub>2</sub> hydrogenation due to their higher reactivity under the reaction temperature. The generated surface hydride are likely covered and protected by CO<sub>2</sub>-derived species under CO<sub>2</sub> hydrogenation conditions. This is supported by our XPS study. Specifically, **Fig. 1d** displays the Ce 3d XPS of fresh, H<sub>2</sub>-treated (at 220 °C and 30 bar), and spent Cu/ceria catalysts. All three catalysts have been purposely exposed to air for an extended period (~ 4 months). As shown in **Fig. 1d**, the spectra of fresh and H<sub>2</sub>-treated sample are similar and both are dominated by Ce<sup>4+</sup> species (~ 93%), suggesting that the formed Ce hydride species under H<sub>2</sub> only condition at 220 °C and 30 bar is not stable after being exposed to air, due to the facile reaction between hydrides and O<sub>2</sub> at room temperature.<sup>39</sup> On the other hand, compared with the fresh and H<sub>2</sub>-treated catalysts, the concentration of Ce<sup>3+</sup> in the spent catalyst is still high (30.72%; **Fig. S7**, and **Table S2**), suggesting that the stable Ce<sup>3+</sup> species observed in the spent catalyst must also co-exist with and thus be protected by surface species derived from the reaction, for instance, surface carbonates.

If that is the case, those carbonate species, in principle, can be removed by heating the spent catalyst in H<sub>2</sub> at elevated temperatures which should also lead to the recovery of Ce<sup>4+</sup> species due to the regeneration of lattice oxygen atoms via reactions such as CO<sub>3</sub><sup>2-</sup> + H<sub>2</sub> → CO/CH<sub>3</sub>OH/H<sub>2</sub>O/CO<sub>2</sub> + O<sub>L</sub> (O<sub>L</sub> stands for lattice oxygen). As expected, as shown in **Fig. S8a**, by heating the spent catalyst in H<sub>2</sub> at elevated temperatures, the concentration of Ce<sup>3+</sup> (Ce<sup>4+</sup>) of the spent catalyst continues to decrease (increase). Such a trend is different from that observed from the H<sub>2</sub>-treated Cu/CeO<sub>2</sub> catalysts. Specifically, for the H<sub>2</sub>-treated catalyst (**Fig. S8b** and **Table S2**), increasing the temperature in H<sub>2</sub> results in a decreasing of the concentration of Ce<sup>4+</sup> from RT to 250 °C. These contrasting observations, again, show the uniqueness of the ceria surface of the spent catalyst and suggest that under the reaction of CO<sub>2</sub> hydrogenation, the selective surface Ce<sup>3+</sup> species could be associated with surface species like carbonates, implying that some carbonate species could be active reaction intermediates for methanol formation over Cu/ceria, as demonstrated in the IR study (discussed in the later section).

Based on these results, a schematic is proposed to show the change of ceria support under the reaction condition (**Fig. 1e**). When the reaction is on and at the initial stage of the reaction, the highly reducing environment and the fast formation of metallic Cu facilitate the formation of Ce<sup>3+</sup> and oxygen vacancy (Ov). At those surface Ce<sup>3+</sup>-Ov pairs, the adsorbed CO<sub>2</sub> could be converted to CO, facilitated by the nearby Cu sites, via the redox reaction mechanism. Correspondingly, the high selectivity of CO (low selectivity of methanol) is observed at t = 0 min (**Fig. S1** and **S5**). With the progressing of the reaction (the induction period), cerium hydride species is formed and detected. Along with the formation of hydride is the evolution of carbonates on the surface of ceria until a steady state is achieved. Those carbonates decorate and stabilize surface Ce<sup>3+</sup> sites, together with diffused H<sup>-</sup>, leading to a unique ceria surface interacting with Cu nanoparticles that result in

high selectivity to methanol (**Fig. S1**). Under the reaction condition, the subtle change of ZnO in Cu/ZnO was also observed by Zabilskiy et al. due to the formation of Zn formate.<sup>4</sup>

These changes observed from ceria lead us to address the following questions: Since Cu sits on the surface of ceria and the particle size of Cu is smaller than ceria, *why is the time-dependent change not observed in Cu and how does Cu interact with ceria under the reaction condition?* The next sections are organized to answer these questions.

### Cu Sites and Dynamic Cu-ceria interaction at the interface

For the above-mentioned question related to Cu, our hypothesis is that the interfacial interaction between ceria and Cu nanoparticle is weak and very dynamic under the highly reducing reaction condition such that any change of Cu sites can be easily overlooked.

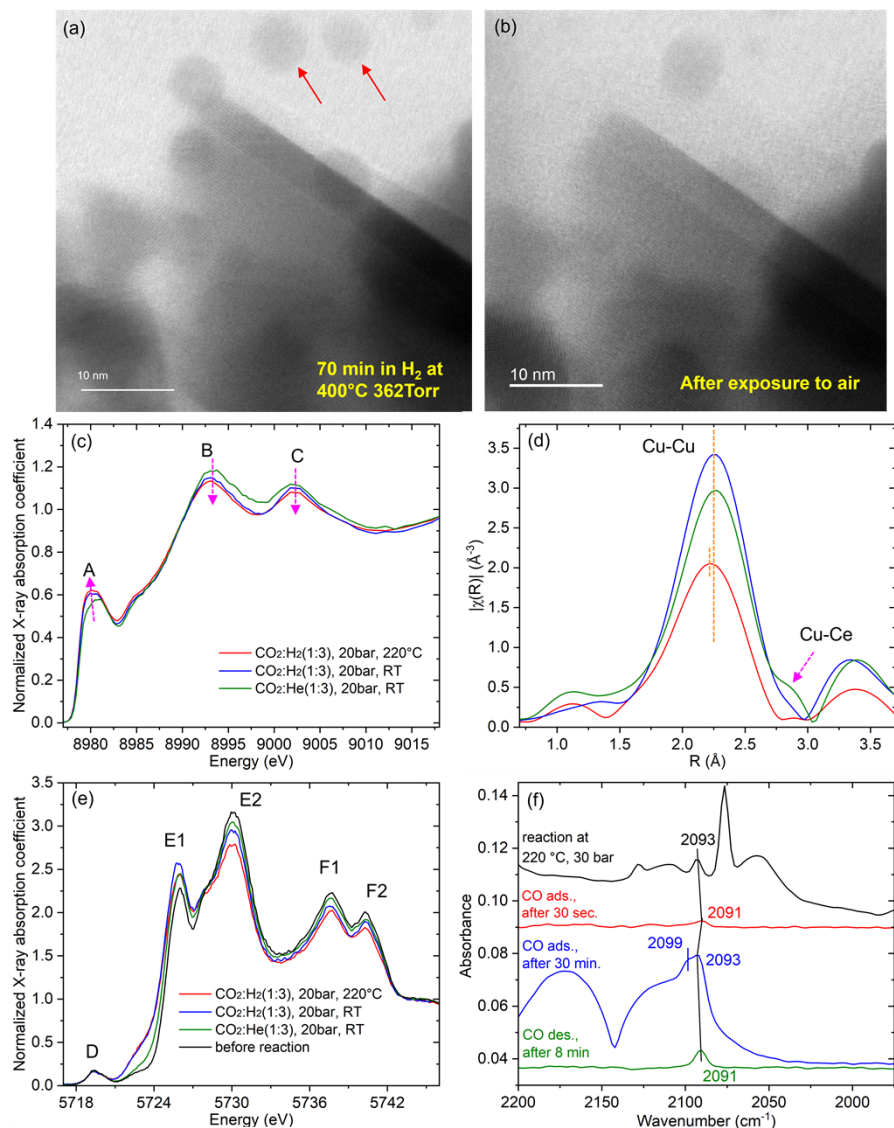


**Figure 2.** (a) BF-STEM image of Cu/ceria collected in H<sub>2</sub> at 400 °C and 362 Torr. The catalyst in (a) was subsequently exposed to air and its BF-STEM image (b) was taken after several days. (c) Cu K edge XANES and (b) EXAFS spectra of the spent Cu/ceria in different conditions and in HERFD mode. Figure a and b share the same legend. (d) Ce L<sub>3</sub> edge HERFD – XANES spectra of the spent Cu/ceria collected in different conditions. (e) The DRIFTS spectra of Cu/ceria under CO<sub>2</sub>:H<sub>2</sub> (1:3)/20bar/220°C, CO (ambient pressure/RT) adsorption and after CO desorption.

To test this hypothesis, in-situ STEM measurements are performed over the Cu/ceria system. As shown in **Fig. 2a**, Cu nanoparticles (~5 nm) which cannot be observed in the as-prepared catalyst (**Fig. S9**) appeared in H<sub>2</sub> at 400 °C. The spherical shape of Cu nanoparticles, different from typically observed truncated cuboctahedral shapes,<sup>40</sup> suggests their weak interaction with ceria support under reducing conditions. In addition, it appears that some Cu nanoparticles (labeled by red arrows) are not intimately contacting with ceria support (more figures in **Fig. S10**). All these indicate that Cu nanoparticles tend to separate from the ceria support in a highly reducing environment at elevated temperatures. The high mobility of these formed Cu nanoparticles is also evidenced by replacing the reactive condition from highly reducing to oxidizing. As shown in **Fig. 2b**, being subsequently exposed to air, many Cu particles seen in **Fig. 2a** (image taken from the same area) disappear and Cu nanoparticles are redispersed on the surface of ceria with time (**Fig. S9**). Agreeing with these observations obtained from in-situ STEM, the estimated average particle size of Cu nanoparticles is ~4.5 nm under the high-pressure reaction condition (based on the Cu-Cu coordination number obtained from EXAFS analysis; **Table S1**),<sup>35</sup> and exposing the spent catalyst to air leads to the oxidation and redispersion of Cu nanoparticles, as suggested by the XAS data (**Fig. S11**). Such an agreement validates the information provided by the in-situ STEM that under the reaction condition, the interaction between Cu and ceria support is weak. Beyond this, the phenomenon of Cu detaching from ceria support under the reducing condition and re-anchoring on the surface of ceria under the oxidizing condition implies that under the reaction condition, the coexistence of H<sub>2</sub> (reducing) and CO<sub>2</sub> (oxidizing) and their adsorption and conversion could lead to dynamic changes at Cu-ceria interface.

To detect the dynamic change of Cu and ceria, high energy resolution fluorescence detected (HERFD) – XAS spectra are collected by exposing the catalyst to different reactive conditions. Compared with conventional XAS, HERFD – XAS spectra show a higher spectral resolution which helps the detection of responses from active sites that are in the minority.<sup>41-47</sup> **Fig. 2c** displays the Cu K edge spectra of Cu/ceria where three peaks, labeled as A, B, and C present in all spectra. Changing the condition from CO<sub>2</sub>:He (1:3)/20bar/RT to CO<sub>2</sub>:H<sub>2</sub> (1:3)/20bar/RT and to CO<sub>2</sub>:H<sub>2</sub> (1:3)/20bar/220°C, the intensity of A gradually increases and those of B and C decrease, suggesting that: 1) a small portion of Cu sites responds to the change of external conditions; 2) those responsive Cu sites tend to gain electrons in H<sub>2</sub> rich conditions and at elevated temperatures.

Along with the change of the local electronic structure of some Cu sites, their local atomic structure changes are also detected under different conditions. **Fig. 2d** exhibits corresponding R-space EXAFS spectra collected under conditions listed in **Fig. 2a**. The k-space EXAFS spectra are shown in **Fig. S12**. All R-space EXAFS spectra show a pronounced Cu-Cu metallic bond at ~2.3 Å. In CO<sub>2</sub>:He (1:3)/20bar/RT condition, an additional contribution at ~2.8 Å can be observed.

This contribution fades after the introduction of H<sub>2</sub> at RT and cannot be detected in the reaction condition (CO<sub>2</sub>:H<sub>2</sub> (1:3)/20bar/220°C). Based on the EXAFS analysis (**Fig. S13** and **Table S1**), it is determined that the peak at ~ 2.8 Å is due to Cu-Ce contribution. In CO<sub>2</sub>:He (1:3)/20bar/RT, the coordination number of Cu-Cu is 9.9±0.7, smaller than that in the reaction condition (CO<sub>2</sub>:H<sub>2</sub> (1:3)/20bar/220°C; CN=10.8±0.3). In the reaction condition (CO<sub>2</sub>:H<sub>2</sub> (1:3)/20bar/220°C), the obtained Cu-Cu bond distance (2.528±0.006 Å) is smaller than that in non-reaction conditions (~ 2.545 Å). These results suggest that CO<sub>2</sub> tends to anchor Cu nanoparticles to ceria while the introduced H<sub>2</sub> tends to break the Cu-ceria interaction and along with it are the restructuring of Cu local structures (increased Cu-Cu coordination number and shortened Cu-Cu bond distance) and gaining of electrons (**Fig. 2a**) of interfacial Cu sites.

A similar trend is observed in the Ce L<sub>3</sub> edge HERFD-XANES spectra, as shown in **Fig. 2e**. All spectra display five prominent features labeled as D, E1, E2, F1 and F2.<sup>42</sup> **Note S1** provides detailed peak assignments and discussion. Compared with the fresh catalyst, regardless of the gas conditions, the spectra of the spent catalyst show higher intensity of E1, lower intensity of E2, F1 and F2, and the appearance of features within 5721- 5724 eV indicate a higher ratio of Ce<sup>3+</sup> species in the spent catalyst (agreeing with results from **Fig. 1a** and **Fig. 1d**). Compared with other gas conditions, CO<sub>2</sub> (CO<sub>2</sub>:He (1:3)/20bar/RT) tends to oxidize a certain amount of Ce<sup>3+</sup> sites. Even at RT, the introduction of H<sub>2</sub> (CO<sub>2</sub>:H<sub>2</sub> (1:3)/20bar/RT) can weaken the CO<sub>2</sub> effect on ceria, as evidenced by the increased E1 and decreased E2, F1, and F2. By elevating the temperature (CO<sub>2</sub>:H<sub>2</sub> (1:3)/20bar/220°C), all peaks including E1, E2, F1, and F2 showed decreased intensity compared with those at RT (CO<sub>2</sub>:H<sub>2</sub> (1:3)/20bar/RT), due to a decrease in the density of unoccupied states of Ce which is associated with decreased ionic character, higher configurational disorder, smaller coordination number of neighbors, and/or weaker interaction with surface adsorbates.<sup>48-50</sup> As a result, under CO<sub>2</sub>:H<sub>2</sub> (1:3)/20bar/220°C, the ceria surface interacts weakly with Cu which also has a higher density of occupied states under the reaction (**Fig. 2c**).

The HERFD – XAS results show that the physical and electronic interaction between Cu and ceria are aggressively manipulated by reactants under high-pressure conditions. Under the reaction condition, Cu-ceria interaction is not only weak but also dynamic which explains the unobserved time-dependent change of Cu.

To reveal the nature of active and selective Cu sites associated with Cu nanoparticles, DRIFTS experiment is performed. We initially intended to analyze the IR spectra collected under the reaction condition. However, as mentioned earlier in the Introduction, some bands associated with gas phase CO<sub>2</sub> overlap with those associated with Cu sites. Specifically, as shown in **Fig. 2f** and **S14**, under the reaction condition (CO<sub>2</sub>:H<sub>2</sub> (1:3)/30bar/220°C), the bands associated with gas phase CO<sub>2</sub> dominate. Particularly, in the wavenumber range of 2200-1900 cm<sup>-1</sup>, where bands due to CO on the surface Cu sites would show up, all appeared bands could also be associated with gas phase CO<sub>2</sub>, making it difficult to reveal surface Cu sites under the reaction condition.<sup>16</sup> To detect surface Cu sites, we therefore switch the feeding of CO<sub>2</sub> and H<sub>2</sub> during the reaction to He in the IR reactor to flush away other gases and remove some active intermediates as well as adsorbed CO so that the associated active Cu sites for methanol and CO formation could be revealed. After dropping the temperature and pressure to RT and ambient pressure, the sample is exposed to gas molecule

CO, and time resolved DRIFTS spectra are collected during the CO adsorption process (**Fig. S15a**). To check the reversibility, subsequently, CO is replaced with He and time resolved DRIFTS spectra during the CO desorption process are also recorded (**Fig. S15a**).

As shown in **Fig. 2f**, after 30 seconds of CO adsorption, a small band at  $2091\text{ cm}^{-1}$  appears. With prolonged exposure time under CO, this band shifts slightly to  $2093\text{ cm}^{-1}$  due to higher CO coverage.<sup>51</sup> In addition, a new band appears at  $2099\text{ cm}^{-1}$ , suggesting that there are at least two types of accessible Cu sites on the surface. These two sites have different electronic or geometric structures and thus lead to different bonding properties with adsorbates such as CO. Specifically, although both  $2093\text{ cm}^{-1}$  and  $2099\text{ cm}^{-1}$  bands are assigned to linearly bonded CO molecules on the surface of metallic Cu sites,<sup>52, 53</sup> compared with the  $2099\text{ cm}^{-1}$  band, the Cu site associated with  $2093\text{ cm}^{-1}$  band has a stronger interaction with CO (based on the observation that it appears first in the CO adsorption process and remains after the desorption of  $2099\text{ cm}^{-1}$  band in the CO desorption process; **Fig. S15a**) due to a stronger back-donation of electron density from the Cu to CO, suggesting that the Cu site responsible for the  $2093\text{ cm}^{-1}$  band has relatively higher electron density.<sup>54</sup> Furthermore, the low intensity of these bands (compared to the gas phase CO bands and the case of CO adsorption over a fairly clean Cu/ceria surface in **Fig. S15b, Note S2**) suggests the low concentration of the two types of accessible Cu sites, agreeing with HERFD – XAS result that there is only a small portion of Cu sites responding to the change of external conditions. These two types of accessible Cu sites are likely involved in CO<sub>2</sub> hydrogenation.

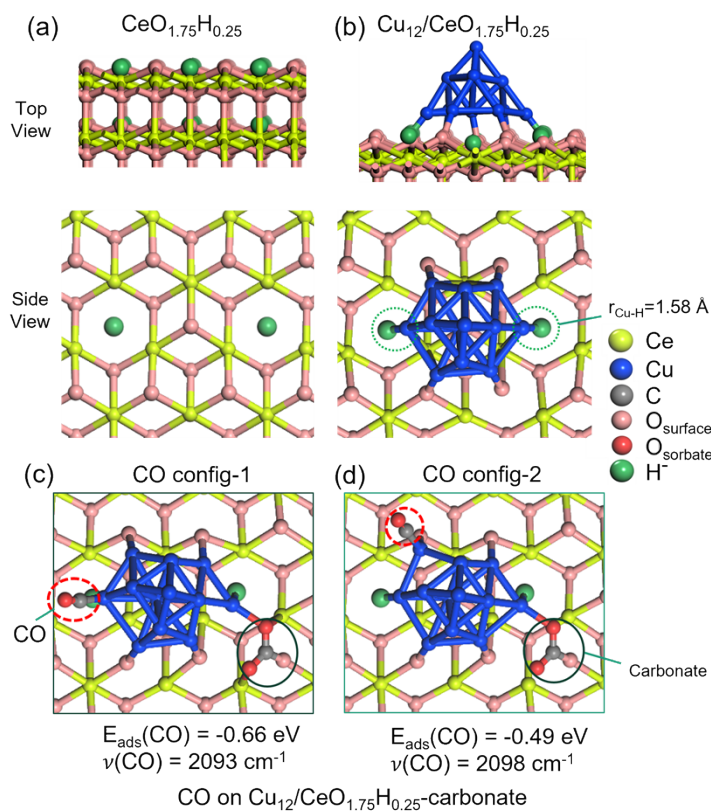


**Figure 3.** (a) DFT modeling of CO adsorption on  $\text{Cu}_{12}/\text{CeO}_{1.75}\text{H}_{0.25}$ -carbonate: (a) the (111) surface of  $\text{CeO}_{1.75}\text{H}_{0.25}$ ; (b) the  $\text{Cu}_{12}$  nanocluster supported on the (111) surface of  $\text{CeO}_{1.75}\text{H}_{0.25}$ ;

(c) the most stable configuration of interfacial CO adsorption on  $\text{Cu}_{12}/\text{CeO}_{1.75}\text{H}_{0.25}$ -carbonate (CO config-1); (d) the next most stable configuration of interfacial CO adsorption on  $\text{Cu}_{12}/\text{CeO}_{1.75}\text{H}_{0.25}$ -carbonate (CO config-2).

To provide more information on these two Cu sites, DFT calculations are performed to model the Cu/ceria interface as well as CO adsorption at the interface. Based on the experimental findings, we construct a bulk cerium oxyhydride with a composition of  $\text{CeO}_{1.75}\text{H}_{0.25}$ ; namely, 1/8 of  $\text{O}^{2-}$  anions are replaced with hydrides and the average oxidate state of Ce is now +3.75 due to  $3/4 \text{ Ce}^{4+}$  and  $1/4 \text{ Ce}^{3+}$ . Then we create the (111) surface from the bulk  $\text{CeO}_{1.75}\text{H}_{0.25}$  and one can see the surface hydrides on the support (**Fig. 3a**). A more detailed analysis of Ce oxidation states was also performed by computing the Bader charges (**Fig. S16, S17**, and **Table S3**). Next, we place a Cu nanoparticle modelled by a hemispherical  $\text{Cu}_{12}$  nanocluster on the surface<sup>55</sup> and optimize the structure (**Fig. 3b**): the interaction between the Cu nanoparticle and the  $\text{CeO}_{1.75}\text{H}_{0.25}$  surface features strong Cu-H bonds of relatively short distances at 1.58 Å, which have been observed in copper-hydride nanoclusters and complexes.<sup>56, 57</sup> We note that the  $\text{Cu}_{12}$  cluster we used to model Cu nanoparticles is much smaller than the ~4.5 nm Cu nanoparticles observed experimentally. Addressing this material gap would be very computationally demanding but could further address the transferability of the conclusions based on the smaller model regarding interfacial charge transfer, CO frequencies, and role of hydrides. A follow-up computational study of larger sizes and different shapes and morphologies is warranted. To simulate the carbonate species, we allow a  $\text{CO}_2$  molecule to react with a surface O site and form a surface carbonate; we test different O sites and found the most stable one being at the interface where one of the carbonate O atom directly bonds with an interface Cu atom (**Fig. S18**). Pristine  $\text{CeO}_{1.75}\text{H}_{0.25}$  surface has 6 out of 16 Ce sites that have oxidation states close to 3+. After  $\text{Cu}_{12}$  cluster adsorption, the number of such sites increase from 6 to 8, and further to 9 following interfacial carbonate adsorption. This gradual increase indicates that both the Cu cluster and the  $\text{CO}_3$  species promote the reduction of  $\text{Ce}^{4+}$  on the surface. Based on the  $\text{Cu}_{12}/\text{CeO}_{1.75}\text{H}_{0.25}$ -carbonate model, we then explore different CO adsorption sites. We find that the most stable site for CO is on top of an interfacial Cu atom that is bonded to a surface hydride (CO config 1; **Fig. 3c**) and the calculated CO vibrational frequency of  $2093 \text{ cm}^{-1}$  closely matches that of the experiment. The next stable interfacial site for CO adsorption (CO config 2; **Fig. 3d**) is on top of a Cu site next to the hydridic Cu and the calculated CO vibrational frequency of  $2098 \text{ cm}^{-1}$  also agrees well with the experiment ( $2099 \text{ cm}^{-1}$ ). To clarify the influence of interfacial carbonate species, we also performed calculations for CO adsorption on  $\text{Cu}_{12}/\text{CeO}_{1.75}\text{H}_{0.25}$  and  $\text{Cu}_{12}/\text{CeO}_{1.75}\text{H}_{0.25}$ -carbonate (**Table S4**). Based on the results obtained on the Bader change of different Cu sites (**Table S5, S6, Fig. S19**), the hydraulic Cu site is relatively electron rich compared with the site next to it.

## Active Reaction Intermediates and Reaction Mechanisms

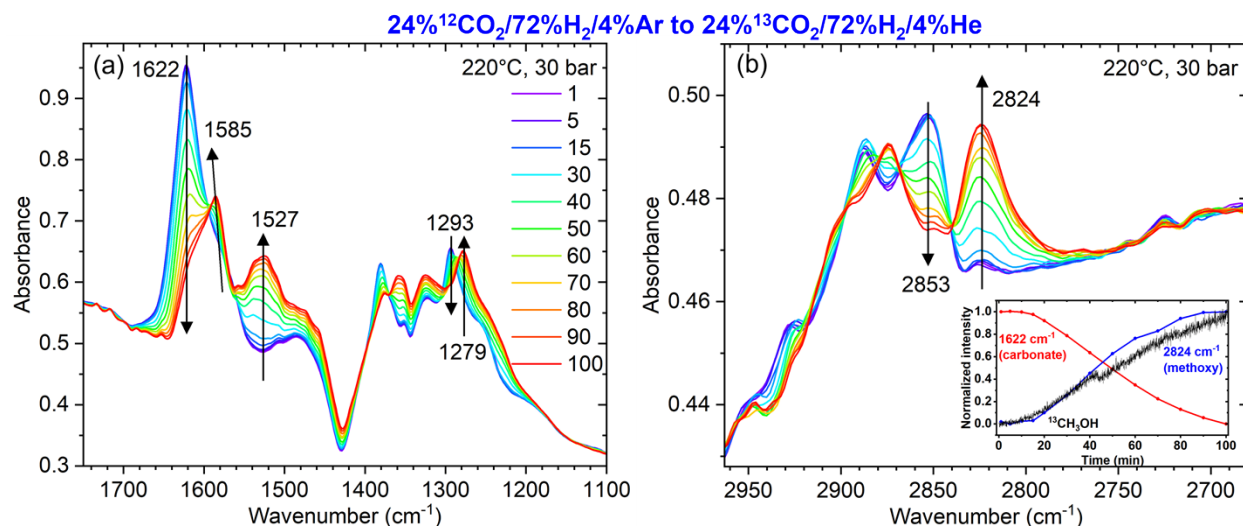


**Figure 4.** The DRIFTS spectra collected at 220 °C and 30 bar upon the switch of the gas environment from 24%<sup>12</sup>CO<sub>2</sub>/72%H<sub>2</sub>/4%Ar to 24%<sup>13</sup>CO<sub>2</sub>/72%H<sub>2</sub>/4%He. Figure a and b share the same legend. Figure b inset shows the changing rate of the bands at 1622 and 2824 cm<sup>-1</sup> and <sup>13</sup>CH<sub>3</sub>OH (detected by using a mass spectrometer) after the <sup>12</sup>C-to-<sup>13</sup>C exchange.

To determine the nature of active reaction intermediates, the intermediates over the Cu/ceria system under the reaction of CO<sub>2</sub> hydrogenation are monitored by performing isotopic switch experiment under steady state condition (switching of the reactant from H<sub>2</sub>+ <sup>12</sup>CO<sub>2</sub> to H<sub>2</sub>+ <sup>13</sup>CO<sub>2</sub>) and collecting IR spectra during the process. As shown in **Fig. 4**, multiple IR bands exist under the reaction condition and generally, they are assigned to carbonate, formate, or methoxy species (**Table S7**).<sup>14, 58-65</sup> Upon <sup>12</sup>CO<sub>2</sub>-to-<sup>13</sup>CO<sub>2</sub> exchange, along with the shift of the bands assigned to carbonate and formate species is the shift of the bands assigned to methoxy species (2853 cm<sup>-1</sup> to 2824 cm<sup>-1</sup>),<sup>61-65</sup> suggesting that both carbonate and formate species could be active intermediates for the formation of methanol over the Cu/ceria system. Despite this, in the C-O region (**Fig. 4a**), the most significant change is observed from the band at 1622 cm<sup>-1</sup>. This band, together with the one at 1293 cm<sup>-1</sup> are assigned to tridentate carbonate and their corresponding <sup>13</sup>C labeled species locate at 1585 and 1279 cm<sup>-1</sup>.<sup>58</sup> Note, after the switch, the weak intensity of 1585 cm<sup>-1</sup> band and the increased 1527 cm<sup>-1</sup> band suggest that 1585 cm<sup>-1</sup> band is also associated with other types of carbonate species or formates.<sup>14, 58-60</sup> By analyzing the intensity change of the bands at 1622 and 2824 cm<sup>-1</sup> and the mass spectrum of <sup>13</sup>CH<sub>3</sub>OH as a function of reaction time, it is found that the decay rate of the unlabeled tridentate carbonate species mirrors the formation rate of the labeled methoxy species and gas phase methanol (**Fig.4b inset**), suggesting that some of the carbonates (not all types of carbonates) could be active reaction intermediates for methanol formation from CO<sub>2</sub> hydrogenation over Cu/ceria.<sup>66-68</sup> In addition, by monitoring the change of surface species after changing the condition from the reaction to either Ar or to H<sub>2</sub> (**Fig. S20**), it is found that the carbonate species at 1622/1293 cm<sup>-1</sup> are more readily responding to the change of gas environment than other species, highlighting the higher reactivity of the carbonate species. The DRIFTS spectra in **Fig. S20**, together with those XPS data (**Fig. S7a**) which show the removal of surface CO<sub>2</sub>-derived species and the recovery of Ce<sup>4+</sup> species in H<sub>2</sub> at elevated temperatures, suggest that those

responding carbonate species are correlated with the selective surface  $\text{Ce}^{3+}$  hydride species created and increased during the reaction condition.

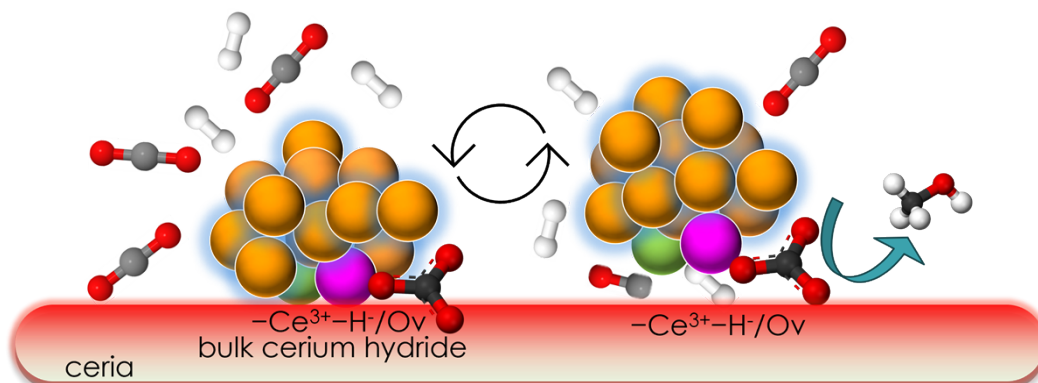


**Figure 5.** A schematic showing the catalytic behavior of Cu/ceria under the reaction. Magenta sphere represents the accessible hydridic Cu site, and the green sphere represents the accessible Cu site that does not directly interact with  $\text{H}^-$ .

Based on the combined results, a schematic (**Fig. 5**) is proposed to show the dynamic catalytic behavior of Cu/ceria for the reaction of  $\text{CO}_2$  hydrogenation to methanol. Under the reaction, there are three types of surface Cu sites. For the first type, the golden ones in the schematic, they are in majority but do not actively participate in the reaction due to their strong bonding with inactive reaction intermediates (as indicated by the low density of Cu sites accessible by CO probing in **Fig. 2f**). For the second type, the green one in the schematic, they do not directly interact with  $\text{H}^-$  site (**Fig. 3d**) and have relatively weak interaction with CO (**Fig. 2f**), which could result in facile CO desorption and contribute to CO selectivity. This assumption is supported by the catalytic behavior of Cu/ceria shown in **Fig. S1**: at the early stage of the reaction when the hydride species are yet to be fully formed, the dominate product is CO. For the third one, the magenta Cu in the schematic, it is bonded to a surface hydride and can stabilize carbonate intermediates (**Fig. S18**). It has unique electronic properties: compared with other interfacial Cu sites, it is relatively electron rich; compared with other surface Cu sites (away from the interface), it is relatively electron deficient (**Table S5**). When combined with the activity data and the change of ceria species (**Fig. 1 and S1**), such local electronic and atomic features of the magenta Cu could be responsible for the selective  $\text{CO}_2$  hydrogenation to methanol. These features could allow the creation of a dynamic interfacial zone at the dominant control of the reactants. For the proceeding of the reaction, the interfacial active carbonate intermediate could be hydrogenated by cerium hydride or by the reactant  $\text{H}_2$ . For the former, an increase of methoxy species (**Fig. S21**), along with the decrease of carbonate species (**Fig. S20a**) is observed when replacing the reaction condition with Ar, implying an active role of hydrides in hydrogenating surface carbonate to methanol. More experimental and theoretical work will be performed to elaborate events occurred at the accessible interfacial Cu sites including the catalytic role of the lattice hydrides.

## Conclusion

This work focuses on revealing the feature of Cu-ceria interface for the reaction of CO<sub>2</sub> hydrogenation to methanol by combining multiple in situ and operando techniques (including STEM, XAS, HERFD – XAS, AP-XPS, neutron scattering and DRIFTS) and DFT calculations/simulations on a working Cu/ceria catalyst. The combined results show the correlated methanol formation with the increase of Ce<sup>3+</sup> species. This unique Ce<sup>3+</sup> species is formed due to the strong effects of reactants: the dissociated H<sub>2</sub> leads to the formation of bulk and surface cerium hydride which is stabilized and protected by carbonate species. The intrusion and chemical bonding of these reactant-derived species at Cu-ceria interface modify and manipulate the Cu-ceria interaction under the reaction with the proceeding of the reaction: the hydrogenation of active carbonates is associated with the dynamic change at Cu-ceria interface. With these insights, to form more of active interfacial site, one may consider the synthesis of Cu core – ceria shell structures and design ceria surfaces enriched with hydride structures and protective carbonate layers.

## Supporting Information

Discussion of Ce L<sub>3</sub> edge HERFD-XANES spectra; catalytic performance; additional characterization data; XAS and XPS data analysis; DFT calculation structures; calculated Bader charge of Ce and Cu sites

## Acknowledgements

This research is supported by the U.S. Department of Energy, Office of Science, Office of Basic Energy Sciences, Chemical Sciences, Geosciences, and Biosciences Division, Catalysis Science program. The sample preparation, reaction test, and STEM studies were conducted as part of a user project at the Center for Nanophase Materials Sciences, which is a Department of Energy, Office of Science User Facility at Oak Ridge National Laboratory. Neutron scattering experiments were conducted at the VISION beamline at ORNL's Spallation Neutron Source, which is supported by the Scientific User Facilities Division, Office of Basic Energy Sciences (BES), U.S. Department of Energy (DOE), under Contract No. DE-AC0500OR22725 with UT Battelle, LLC. XAS data were collected the beamlines 4-2, 9-3, and 15-2 of the Stanford Synchrotron Radiation Lighthouse (SSRL), which is a U.S. Department of Energy Office of Science user facility at the SLAC National Laboratory, which is supported by the U.S. Department of Energy, Office of Science, Office of Basic Energy Sciences under Contract No. DE-AC02-76SF00515. The XAS experiments were performed by collaborating with Co-ACCESS, which is part of the SUNCAT Center for Interface Science and Catalysis and supported by the U.S. Department of Energy, Office of Basic Energy Sciences, Chemical Sciences, Geosciences and Biosciences Division. This manuscript has been authored by UT-Battelle, LLC under Contract No. DE-AC05-00OR22725 with the U.S. Department of Energy. The United States Government retains and the publisher, by accepting the article for publication, acknowledges that the United States Government retains a

non-exclusive, paid-up, irrevocable, world-wide license to publish or reproduce the published form of this manuscript, or allow others to do so, for United States Government purposes. The Department of Energy will provide public access to these results of federally sponsored research in accordance with the DOE Public Access Plan (<http://energy.gov/downloads/doe-public-access-plan>).

## References

- (1) Jiang, X.; Nie, X.; Guo, X.; Song, C.; Chen, J. G. Recent Advances in Carbon Dioxide Hydrogenation to Methanol via Heterogeneous Catalysis. *Chemical Reviews* **2020**, *120* (15), 7984-8034. DOI: 10.1021/acs.chemrev.9b00723.
- (2) Kanuri, S.; Roy, S.; Chakraborty, C.; Datta, S. P.; Singh, S. A.; Dinda, S. An insight of CO<sub>2</sub> hydrogenation to methanol synthesis: Thermodynamics, catalysts, operating parameters, and reaction mechanism. *International Journal of Energy Research* **2021**, *46* (5), 5503-5522. DOI: <https://doi.org/10.1002/er.7562>.
- (3) Kattel, S.; Ramírez, P. J.; Chen, J. G.; Rodriguez, J. A.; Liu, P. Active sites for CO<sub>2</sub> hydrogenation to methanol on Cu/ZnO catalysts. *Science* **2017**, *355* (6331), 1296-1299. DOI: doi:10.1126/science.aal3573.
- (4) Zabilskiy, M.; Sushkevich, V. L.; Palagin, D.; Newton, M. A.; Krumeich, F.; van Bokhoven, J. A. The unique interplay between copper and zinc during catalytic carbon dioxide hydrogenation to methanol. *Nature Communications* **2020**, *11* (1), 2409. DOI: 10.1038/s41467-020-16342-1.
- (5) Liang, H.; Zhang, G.; Li, Z.; Zhang, Y.; Fu, P. Catalytic hydrogenation of CO<sub>2</sub> to methanol over Cu-based catalysts: Active sites profiling and regulation strategy as well as reaction pathway exploration. *Fuel Processing Technology* **2023**, *252*, 107995. DOI: <https://doi.org/10.1016/j.fuproc.2023.107995>.
- (6) Kandemir, T.; Girgsdies, F.; Hansen, T. C.; Liss, K.-D.; Kasatkin, I.; Kunkes, E. L.; Wowsnick, G.; Jacobsen, N.; Schlögl, R.; Behrens, M. In Situ Study of Catalytic Processes: Neutron Diffraction of a Methanol Synthesis Catalyst at Industrially Relevant Pressure. *Angewandte Chemie International Edition* **2013**, *52* (19), 5166-5170. DOI: <https://doi.org/10.1002/anie.201209539>.
- (7) Li, K.; Chen, J. G. CO<sub>2</sub> Hydrogenation to Methanol over ZrO<sub>2</sub>-Containing Catalysts: Insights into ZrO<sub>2</sub> Induced Synergy. *ACS Catalysis* **2019**, *9* (9), 7840-7861. DOI: 10.1021/acscatal.9b01943.
- (8) Graciani, J.; Mudiyansele, K.; Xu, F.; Baber, A. E.; Evans, J.; Senanayake, S. D.; Stacchiola, D. J.; Liu, P.; Hrbek, J.; Sanz, J. F.; et al. Highly active copper-ceria and copper-ceria-titania catalysts for methanol synthesis from CO<sub>2</sub>. *Science* **2014**, *345* (6196), 546-550. DOI: doi:10.1126/science.1253057.

- (9) Senanayake, S. D.; Ramírez, P. J.; Waluyo, I.; Kundu, S.; Mudiyanse, K.; Liu, Z.; Liu, Z.; Axnanda, S.; Stacchiola, D. J.; Evans, J.; et al. Hydrogenation of CO<sub>2</sub> to Methanol on CeO<sub>x</sub>/Cu(111) and ZnO/Cu(111) Catalysts: Role of the Metal–Oxide Interface and Importance of Ce<sup>3+</sup> Sites. *The Journal of Physical Chemistry C* **2016**, *120* (3), 1778-1784. DOI: 10.1021/acs.jpcc.5b12012.
- (10) Wang, Y.; Kattel, S.; Gao, W.; Li, K.; Liu, P.; Chen, J. G.; Wang, H. Exploring the ternary interactions in Cu–ZnO–ZrO<sub>2</sub> catalysts for efficient CO<sub>2</sub> hydrogenation to methanol. *Nature Communications* **2019**, *10* (1), 1166. DOI: 10.1038/s41467-019-09072-6.
- (11) Wu, C.; Lin, L.; Liu, J.; Zhang, J.; Zhang, F.; Zhou, T.; Rui, N.; Yao, S.; Deng, Y.; Yang, F.; et al. Inverse ZrO<sub>2</sub>/Cu as a highly efficient methanol synthesis catalyst from CO<sub>2</sub> hydrogenation. *Nature Communications* **2020**, *11* (1), 5767. DOI: 10.1038/s41467-020-19634-8.
- (12) Zhu, Y.; Zheng, J.; Ye, J.; Cui, Y.; Koh, K.; Kovarik, L.; Camaioni, D. M.; Fulton, J. L.; Truhlar, D. G.; Neurock, M.; et al. Copper-zirconia interfaces in UiO-66 enable selective catalytic hydrogenation of CO<sub>2</sub> to methanol. *Nature Communications* **2020**, *11* (1), 5849. DOI: 10.1038/s41467-020-19438-w.
- (13) Amann, P.; Klötzer, B.; Degerman, D.; Köpfle, N.; Götsch, T.; Lömker, P.; Rameshan, C.; Ploner, K.; Bikaljevic, D.; Wang, H.-Y.; et al. The state of zinc in methanol synthesis over a Zn/ZnO/Cu(211) model catalyst. *Science* **2022**, *376* (6593), 603-608. DOI: doi:10.1126/science.abj7747.
- (14) He, Y.; Li, Y.; Lei, M.; Polo-Garzon, F.; Perez-Aguilar, J.; Bare, S. R.; Formo, E.; Kim, H.; Daemen, L.; Cheng, Y.; et al. Significant Roles of Surface Hydrides in Enhancing the Performance of Cu/BaTiO<sub>2.8</sub>H<sub>0.2</sub> Catalyst for CO<sub>2</sub> Hydrogenation to Methanol. *Angewandte Chemie International Edition* **2024**, *63* (1), e202313389. DOI: <https://doi.org/10.1002/anie.202313389>.
- (15) Li, Y.; Wu, Z. A review of in situ/operando studies of heterogeneous catalytic hydrogenation of CO<sub>2</sub> to methanol. *Catalysis Today* **2023**, *420*, 114029. DOI: <https://doi.org/10.1016/j.cattod.2023.02.006>.
- (16) Fehr, S. M.; Krossing, I. Spectroscopic Signatures of Pressurized Carbon Dioxide in Diffuse Reflectance Infrared Spectroscopy of Heterogeneous Catalysts. *ChemCatChem* **2020**, *12* (9), 2622-2629. DOI: <https://doi.org/10.1002/cctc.201902038>.
- (17) Divins, N. J.; Kordus, D.; Timoshenko, J.; Sinev, I.; Zegkinoglou, I.; Bergmann, A.; Chee, S. W.; Widrinna, S.; Karşlıoğlu, O.; Mistry, H.; et al. Operando high-pressure investigation of size-controlled CuZn catalysts for the methanol synthesis reaction. *Nature Communications* **2021**, *12* (1), 1435. DOI: 10.1038/s41467-021-21604-7.
- (18) Tsoukalou, A.; Abdala, P. M.; Stoian, D.; Huang, X.; Willinger, M.-G.; Fedorov, A.; Müller, C. R. Structural Evolution and Dynamics of an In<sub>2</sub>O<sub>3</sub> Catalyst for CO<sub>2</sub> Hydrogenation to Methanol: An Operando XAS-XRD and In Situ TEM Study. *Journal of the American Chemical Society* **2019**, *141* (34), 13497-13505. DOI: 10.1021/jacs.9b04873.

- (19) Tsoukalou, A.; Abdala, P. M.; Armutlulu, A.; Willinger, E.; Fedorov, A.; Müller, C. R. Operando X-ray Absorption Spectroscopy Identifies a Monoclinic ZrO<sub>2</sub>:In Solid Solution as the Active Phase for the Hydrogenation of CO<sub>2</sub> to Methanol. *ACS Catalysis* **2020**, *10* (17), 10060-10067. DOI: 10.1021/acscatal.0c01968.
- (20) Zabilskiy, M.; Sushkevich, V. L.; Newton, M. A.; Krumeich, F.; Nachtegaal, M.; van Bokhoven, J. A. Mechanistic Study of Carbon Dioxide Hydrogenation over Pd/ZnO-Based Catalysts: The Role of Palladium–Zinc Alloy in Selective Methanol Synthesis. *Angewandte Chemie International Edition* **2021**, *60* (31), 17053-17059. DOI: <https://doi.org/10.1002/anie.202103087>.
- (21) Zhang, F.; Liu, Z.; Chen, X.; Rui, N.; Betancourt, L. E.; Lin, L.; Xu, W.; Sun, C.-j.; Abeykoon, A. M. M.; Rodriguez, J. A.; et al. Effects of Zr Doping into Ceria for the Dry Reforming of Methane over Ni/CeZrO<sub>2</sub> Catalysts: In Situ Studies with XRD, XAFS, and AP-XPS. *ACS Catalysis* **2020**, *10* (5), 3274-3284. DOI: 10.1021/acscatal.9b04451.
- (22) Palomino, R. M.; Hamlyn, R.; Liu, Z.; Grinter, D. C.; Waluyo, I.; Rodriguez, J. A.; Senanayake, S. D. Interfaces in heterogeneous catalytic reactions: Ambient pressure XPS as a tool to unravel surface chemistry. *Journal of Electron Spectroscopy and Related Phenomena* **2017**, *221*, 28-43. DOI: <https://doi.org/10.1016/j.elspec.2017.04.006>.
- (23) Seeger, P. A.; Daemen, L. L.; Larese, J. Z. Resolution of VISION, a crystal-analyzer spectrometer. *Nuclear Inst. and Methods in Physics Research, A* **2009**, *604* (3), 719-728. DOI: 10.1016/j.nima.2009.03.204.
- (24) Hoffman, A. S.; Singh, J. A.; Bent, S. F.; Bare, S. R. In situ observation of phase changes of a silica-supported cobalt catalyst for the Fischer-Tropsch process by the development of a synchrotron-compatible in situ/operando powder X-ray diffraction cell. *Journal of Synchrotron Radiation* **2018**, *25* (6), 1673-1682. DOI: doi:10.1107/S1600577518013942.
- (25) Kresse, G.; Furthmüller, J. Efficiency of ab-initio total energy calculations for metals and semiconductors using a plane-wave basis set. *Computational Materials Science* **1996**, *6* (1), 15-50. DOI: [https://doi.org/10.1016/0927-0256\(96\)00008-0](https://doi.org/10.1016/0927-0256(96)00008-0).
- (26) Kresse, G.; Furthmüller, J. Efficient iterative schemes for ab initio total-energy calculations using a plane-wave basis set. *Physical Review B* **1996**, *54* (16), 11169-11186. DOI: 10.1103/PhysRevB.54.11169.
- (27) Perdew, J. P.; Burke, K.; Ernzerhof, M. Generalized Gradient Approximation Made Simple. *Physical Review Letters* **1996**, *77* (18), 3865-3868. DOI: 10.1103/PhysRevLett.77.3865.
- (28) Blöchl, P. E. Projector augmented-wave method. *Physical Review B* **1994**, *50* (24), 17953-17979. DOI: 10.1103/PhysRevB.50.17953.
- (29) Kresse, G.; Joubert, D. From ultrasoft pseudopotentials to the projector augmented-wave method. *Physical Review B* **1999**, *59* (3), 1758-1775. DOI: 10.1103/PhysRevB.59.1758.

- (30) Dion, M.; Rydberg, H.; Schröder, E.; Langreth, D. C.; Lundqvist, B. I. Van der Waals Density Functional for General Geometries. *Physical Review Letters* **2004**, *92* (24), 246401. DOI: 10.1103/PhysRevLett.92.246401.
- (31) K. G, L.; Kundappaden, I.; Chatanathodi, R. A DFT study of CO adsorption on pt (111) using van der Waals functionals. *Surface Science* **2019**, *681*, 143-148. DOI: <https://doi.org/10.1016/j.susc.2018.12.001>.
- (32) Li, Y.; Wang, H.; Song, H.; Rui, N.; Kottwitz, M.; Senanayake, S. D.; Nuzzo, R. G.; Wu, Z.; Jiang, D.-e.; Frenkel, A. I. Active sites of atomically dispersed Pt supported on Gd-doped ceria with improved low temperature performance for CO oxidation. *Chemical Science* **2023**, *14* (44), 12582-12588, 10.1039/D3SC03988A. DOI: 10.1039/D3SC03988A.
- (33) Ban, T.; Yu, X.-Y.; Kang, H.-Z.; Huang, Z.-Q.; Li, J.; Chang, C.-R. Design of SA-FLP Dual Active Sites for Nonoxidative Coupling of Methane. *ACS Catalysis* **2023**, *13* (2), 1299-1309. DOI: 10.1021/acscatal.2c04479.
- (34) Yang, W.; Song, H.; Zhang, L.; Zhang, J.; Polo-Garzon, F.; Wang, H.; Meyer, H., III; Jiang, D.-e.; Wu, Z.; Li, Y. Active Palladium Structures on Ceria Obtained by Tuning Pd–Pd Distance for Efficient Methane Combustion. *ACS Catalysis* **2024**, *14* (21), 16459-16468. DOI: 10.1021/acscatal.4c04985.
- (35) Li, Y.; Frenkel, A. I. Metal Nanocatalysts. In *XAFS Techniques for Catalysts, Nanomaterials, and Surfaces*, Iwasawa, Y., Asakura, K., Tada, M. Eds.; Springer International Publishing, 2017; pp 273-298.
- (36) Phokha, S.; Swatsitang, E.; Maensiri, S. Room-temperature ferromagnetism in pure CeO<sub>2</sub> nanoparticles prepared by a simple direct thermal decomposition. *Electronic Materials Letters* **2015**, *11* (6), 1012-1020. DOI: 10.1007/s13391-015-4164-4.
- (37) Booth, C. H.; Walter, M. D.; Daniel, M.; Lukens, W. W.; Andersen, R. A. Self-Contained Kondo Effect in Single Molecules. *Physical Review Letters* **2005**, *95* (26), 267202. DOI: 10.1103/PhysRevLett.95.267202.
- (38) Wu, T.-S.; Syu, L.-Y.; Lin, B.-H.; Weng, S.-C.; Jeng, H.-T.; Huang, Y.-S.; Soo, Y.-L. Reduction of dopant ions and enhancement of magnetic properties by UV irradiation in Ce-doped TiO<sub>2</sub>. *Scientific Reports* **2021**, *11* (1), 7668. DOI: 10.1038/s41598-021-87115-z.
- (39) Wu, Z.; Cheng, Y.; Tao, F.; Daemen, L.; Foo, G. S.; Nguyen, L.; Zhang, X.; Beste, A.; Ramirez-Cuesta, A. J. Direct Neutron Spectroscopy Observation of Cerium Hydride Species on a Cerium Oxide Catalyst. *Journal of the American Chemical Society* **2017**, *139* (28), 9721-9727. DOI: 10.1021/jacs.7b05492.
- (40) Li, Y.; Kottwitz, M.; Vincent, J. L.; Enright, M. J.; Liu, Z.; Zhang, L.; Huang, J.; Senanayake, S. D.; Yang, W.-C. D.; Crozier, P. A.; et al. Dynamic structure of active sites in ceria-supported Pt catalysts for the water gas shift reaction. *Nature Communications* **2021**, *12* (1), 914. DOI: 10.1038/s41467-021-21132-4.

- (41) Günter, T.; Carvalho, H. W. P.; Doronkin, D. E.; Sheppard, T.; Glatzel, P.; Atkins, A. J.; Rudolph, J.; Jacob, C. R.; Casapu, M.; Grunwaldt, J.-D. Structural snapshots of the SCR reaction mechanism on Cu-SSZ-13. *Chemical Communications* **2015**, *51* (44), 9227-9230, 10.1039/C5CC01758K. DOI: 10.1039/C5CC01758K.
- (42) Li, Y.; Kraynis, O.; Kas, J.; Weng, T.-C.; Sokaras, D.; Zacharowicz, R.; Lubomirsky, I.; Frenkel, A. I. Geometry of electromechanically active structures in Gadolinium - doped Cerium oxides. *AIP Advances* **2016**, *6* (5). DOI: 10.1063/1.4952645 (accessed 6/4/2024).
- (43) Elsen, A.; Jung, U.; Vila, F.; Li, Y.; Safonova, O. V.; Thomas, R.; Tromp, M.; Rehr, J. J.; Nuzzo, R. G.; Frenkel, A. I. Intracluster Atomic and Electronic Structural Heterogeneities in Supported Nanoscale Metal Catalysts. *The Journal of Physical Chemistry C* **2015**, *119* (45), 25615-25627. DOI: 10.1021/acs.jpcc.5b08267.
- (44) Hämäläinen, K.; Siddons, D. P.; Hastings, J. B.; Berman, L. E. Elimination of the inner-shell lifetime broadening in x-ray-absorption spectroscopy. *Physical Review Letters* **1991**, *67* (20), 2850-2853. DOI: 10.1103/PhysRevLett.67.2850.
- (45) Safonova, O. V.; Tromp, M.; van Bokhoven, J. A.; de Groot, F. M. F.; Evans, J.; Glatzel, P. Identification of CO Adsorption Sites in Supported Pt Catalysts Using High-Energy-Resolution Fluorescence Detection X-ray Spectroscopy. *The Journal of Physical Chemistry B* **2006**, *110* (33), 16162-16164. DOI: 10.1021/jp063416t.
- (46) van Bokhoven, J. A.; Louis, C.; Miller, J. T.; Tromp, M.; Safonova, O. V.; Glatzel, P. Activation of Oxygen on Gold/Alumina Catalysts: In Situ High-Energy-Resolution Fluorescence and Time-Resolved X-ray Spectroscopy. *Angewandte Chemie International Edition* **2006**, *45* (28), 4651-4654. DOI: <https://doi.org/10.1002/anie.200601184>.
- (47) de Groot, F. M. F.; Krisch, M. H.; Vogel, J. Spectral sharpening of the Pt L edges by high-resolution x-ray emission. *Physical Review B* **2002**, *66* (19), 195112. DOI: 10.1103/PhysRevB.66.195112.
- (48) Zhang, F.; Wang, P.; Koberstein, J.; Khalid, S.; Chan, S.-W. Cerium oxidation state in ceria nanoparticles studied with X-ray photoelectron spectroscopy and absorption near edge spectroscopy. *Surface Science* **2004**, *563* (1), 74-82. DOI: <https://doi.org/10.1016/j.susc.2004.05.138>.
- (49) Korobko, R.; Patlolla, A.; Kossoy, A.; Wachtel, E.; Tuller, H. L.; Frenkel, A. I.; Lubomirsky, I. Giant Electrostriction in Gd-Doped Ceria. *Advanced Materials* **2012**, *24* (43), 5857-5861. DOI: <https://doi.org/10.1002/adma.201202270>.
- (50) Korobko, R.; Lerner, A.; Li, Y.; Wachtel, E.; Frenkel, A. I.; Lubomirsky, I. In-situ extended X-ray absorption fine structure study of electrostriction in Gd doped ceria. *Applied Physics Letters* **2015**, *106* (4). DOI: 10.1063/1.4906857 (accessed 6/4/2024).
- (51) Roiaz, M.; Falivene, L.; Rameshan, C.; Cavallo, L.; Kozlov, S. M.; Rupprechter, G. Roughening of Copper (100) at Elevated CO Pressure: Cu Adatom and Cluster Formation Enable

CO Dissociation. *The Journal of Physical Chemistry C* **2019**, *123* (13), 8112-8121. DOI: 10.1021/acs.jpcc.8b07668.

(52) Gunathunge, C. M.; Li, J.; Li, X.; Waegele, M. M. Surface-Adsorbed CO as an Infrared Probe of Electrocatalytic Interfaces. *ACS Catalysis* **2020**, *10* (20), 11700-11711. DOI: 10.1021/acscatal.0c03316.

(53) Topsøe, N.-Y.; Topsøe, H. FTIR studies of dynamic surface structural changes in Cu-based methanol synthesis catalysts. Received 4 December 1997; accepted 20 March 1998. *Journal of Molecular Catalysis A: Chemical* **1999**, *141* (1), 95-105. DOI: [https://doi.org/10.1016/S1381-1169\(98\)00253-2](https://doi.org/10.1016/S1381-1169(98)00253-2).

(54) Zhang, Y.; Chen, Y.; Wang, X.; Feng, Y.; Dai, Z.; Cheng, M.; Zhang, G. Low-coordinated copper facilitates the \*CH<sub>2</sub>CO affinity at enhanced rectifying interface of Cu/Cu<sub>2</sub>O for efficient CO<sub>2</sub>-to-multicarbon alcohols conversion. *Nature Communications* **2024**, *15* (1), 5172. DOI: 10.1038/s41467-024-49247-4.

(55) Wan, Q.; Wei, F.; Wang, Y.; Wang, F.; Zhou, L.; Lin, S.; Xie, D.; Guo, H. Single atom detachment from Cu clusters, and diffusion and trapping on CeO<sub>2</sub>(111): implications in Ostwald ripening and atomic redispersion. *Nanoscale* **2018**, *10* (37), 17893-17901, 10.1039/C8NR06232C. DOI: 10.1039/C8NR06232C.

(56) Fritsch, L.; Rehsies, P.; Barakat, W.; Estes, D. P.; Bauer, M. Detection and Characterization of Hydride Ligands in Copper Complexes by Hard X-Ray Spectroscopy. *Chemistry – A European Journal* **2024**, *30* (36), e202400357. DOI: <https://doi.org/10.1002/chem.202400357>.

(57) Edwards, A. J.; Dhayal, R. S.; Liao, P.-K.; Liao, J.-H.; Chiang, M.-H.; Piltz, R. O.; Kahlal, S.; Saillard, J.-Y.; Liu, C. W. Chinese Puzzle Molecule: A 15 Hydride, 28 Copper Atom Nanoball. *Angewandte Chemie International Edition* **2014**, *53* (28), 7214-7218. DOI: <https://doi.org/10.1002/anie.201403324>.

(58) Vayssilov, G. N.; Mihaylov, M.; Petkov, P. S.; Hadjiivanov, K. I.; Neyman, K. M. Reassignment of the Vibrational Spectra of Carbonates, Formates, and Related Surface Species on Ceria: A Combined Density Functional and Infrared Spectroscopy Investigation. *The Journal of Physical Chemistry C* **2011**, *115* (47), 23435-23454. DOI: 10.1021/jp208050a.

(59) Fehr, S. M.; Nguyen, K.; Krossing, I. Realistic Operando-DRIFTS Studies on Cu/ZnO Catalysts for CO<sub>2</sub> Hydrogenation to Methanol – Direct Observation of Mono-ionized Defect Sites and Implications for Reaction Intermediates. *ChemCatChem* **2022**, *14* (3), e202101500. DOI: <https://doi.org/10.1002/cctc.202101500>.

(60) Lustemberg, P. G.; Bosco, M. V.; Bonivardi, A.; Busnengo, H. F.; Ganduglia-Pirovano, M. V. Insights into the Nature of Formate Species in the Decomposition and Reaction of Methanol over Cerium Oxide Surfaces: A Combined Infrared Spectroscopy and Density Functional Theory Study. *The Journal of Physical Chemistry C* **2015**, *119* (37), 21452-21464. DOI: 10.1021/acs.jpcc.5b05070.

- (61) Sugiyama, H.; Miyazaki, M.; Sasase, M.; Kitano, M.; Hosono, H. Room-Temperature CO<sub>2</sub> Hydrogenation to Methanol over Air-Stable hcp-PdMo Intermetallic Catalyst. *Journal of the American Chemical Society* **2023**, *145* (17), 9410-9416. DOI: 10.1021/jacs.2c13801.
- (62) Hu, J.; Yu, L.; Deng, J.; Wang, Y.; Cheng, K.; Ma, C.; Zhang, Q.; Wen, W.; Yu, S.; Pan, Y.; et al. Sulfur vacancy-rich MoS<sub>2</sub> as a catalyst for the hydrogenation of CO<sub>2</sub> to methanol. *Nature Catalysis* **2021**, *4* (3), 242-250. DOI: 10.1038/s41929-021-00584-3.
- (63) Uvdal, P.; Weldon, M. K.; Friend, C. M. Adsorbate symmetry and Fermi resonances of methoxide adsorbed on Mo(110) as studied by surface infrared spectroscopy. *Physical Review B* **1994**, *50* (16), 12258-12261. DOI: 10.1103/PhysRevB.50.12258.
- (64) Ojelade, O. A.; Zaman, S. F. A Review on Pd Based Catalysts for CO<sub>2</sub> Hydrogenation to Methanol: In-Depth Activity and DRIFTS Mechanistic Study. *Catalysis Surveys from Asia* **2020**, *24* (1), 11-37. DOI: 10.1007/s10563-019-09287-z.
- (65) Badri, A.; Binet, C.; Lavalley, J.-C. Use of methanol as an IR molecular probe to study the surface of polycrystalline ceria. *Journal of the Chemical Society, Faraday Transactions* **1997**, *93* (6), 1159-1168, 10.1039/A606628C. DOI: 10.1039/A606628C.
- (66) Wang, W.; Qu, Z.; Song, L.; Fu, Q. CO<sub>2</sub> hydrogenation to methanol over Cu/CeO<sub>2</sub> and Cu/ZrO<sub>2</sub> catalysts: Tuning methanol selectivity via metal-support interaction. *Journal of Energy Chemistry* **2020**, *40*, 22-30. DOI: <https://doi.org/10.1016/j.jechem.2019.03.001>.
- (67) Vergara, T.; Gómez, D.; Lacerda de Oliveira Campos, B.; Herrera Delgado, K.; Jiménez, R.; Karelavic, A. Disclosing the Reaction Mechanism of CO<sub>2</sub> Hydrogenation to Methanol over CuCeOx/TiO<sub>2</sub>: A Combined Kinetic, Spectroscopic, and Isotopic Study. *ACS Catalysis* **2023**, *13* (22), 14699-14715. DOI: 10.1021/acscatal.3c04243.
- (68) Zhu, J.; Su, Y.; Chai, J.; Muravev, V.; Kosinov, N.; Hensen, E. J. M. Mechanism and Nature of Active Sites for Methanol Synthesis from CO/CO<sub>2</sub> on Cu/CeO<sub>2</sub>. *ACS Catalysis* **2020**, *10* (19), 11532-11544. DOI: 10.1021/acscatal.0c02909.

For Table of Contents Only

